RSC Advances

PAPER

View Article Online
View Journal | View Issue

Cite this: *RSC Adv.*, 2021, **11**, 9336

Fabrication of TiO_2 microspikes for highly efficient intracellular delivery by pulse laser-assisted photoporation

L. Mohan, [ab] Srabani Kar, [ac] Pallab Sinha Mahapatra, [d] Moeto Nagai [b] and Tuhin Subhra Santra *[a]

The introduction of foreign cargo into living cells with high delivery efficiency and cell viability is a challenge in cell biology and biomedical research. Here, we demonstrate a nanosecond pulse laser-activated photoporation for highly efficient intracellular delivery using titanium dioxide (TiO_2) microspikes as a substratum. The TiO_2 microspikes were formed on titanium (Ti) substrate using an electrochemical anodization process. Cells were cultured on top of the TiO_2 microspikes as a monolayer, and the biomolecule was added. Due to pulse laser exposure of the TiO_2 microspike–cell membrane interface, the microspikes heat up and induce cavitation bubbles, which rapidly grow, coalesce and collapse to induce explosion, resulting in very strong fluid flow at the cell membrane surface. Thus, the cell plasma membrane disrupts and creates transient nanopores, allowing delivery of biomolecules into cells by a simple diffusion process. By this technique, we successfully delivered propidium iodide (PI) dye in HeLa cells with high delivery efficiency (93%) and high cell viability (98%) using 7 mJ pulse energy at 650 nm wavelength. Thus, our TiO_2 microspike-based platform is compact, easy to use, and potentially applicable for therapeutic and diagnostic purposes.

Received 18th November 2020
Accepted 15th February 2021

DOI: 10.1039/d0ra09785c

rsc.li/rsc-advances

1. Introduction

Titanium (Ti) and Ti-based alloys are commonly used for dental prosthetics and orthopedic applications owing to their higher mechanical strength, biocompatibility, corrosion resistance, and micro/nanostructured features.[1–3] In recent years, micro/nanotechnology has emerged as a vital research area with various applications. Micro/nanostructured metal oxide synthesis has gained significant research interest due to its favorable application for micro and nanodevice fabrication.[4] The micro/nanostructures on titanium metal are advantageous, as they are less costly, possess a tailorable surface chemistry, well-ordered micro/nanostructures, flexibility, high surface area, mechanical rigidity, and outstanding biocompatibility.[5–8] Nanostructured materials such as nanorods, nanowires, nanoparticles, nanofilms, nanotubes, *etc.*, have been constructed due to their promising applications in numerous fields. The electrochemical formation of porous/micro/nanostructures for different types of materials such as Al,[9] Fe,[10] Hf,[11] Mg,[12] Nb,[13] Ni,[14] Ru,[15] Si,[16] W,[17] and Ti[18–20] already exists. Besides the metal substrate, nanostructures can also be formed using anodization on Ti alloy substrates, such as Ti–6Al–7Nb,[8,21] Ni–Ti,[22,23] Ti–6Al–4V,[7] Ti13Nb13Zr[24,25] and Ti15Mo.[26] Among the many nanostructured oxide materials, TiO_2-based nanostructures have significant characteristics, such as improved ion-exchangeable ability, photocatalytic properties, environmental safety, and nontoxicity. However, the formation of TiO_2 microspikes on titanium substrate by electrochemical anodization process and their biomedical applications, such as drug delivery or intracellular delivery, have not yet been studied.

Intracellular delivery is a critical task in nanomedicine-based drug delivery. The past few decades have witnessed the progress of nanomedicine from biologically inert materials to smart systems, intended at evolving *in vivo* functionality. Probing the nano-bio interactions and the necessary functionalities at the molecular, cellular, and tissue levels are often ignored. Development towards a response to these queries will yield more effective chemo-physical approaches.[32] The intracellular delivery of foreign macromolecules into cells is essential to basic biomedical research and the analysis of many diseases.[27–31] The capability to transport foreign macromolecules into living cells with high transfection efficacy and high cell viability is of great interest in cell biology for the applications in therapeutics, diagnostics, and drug delivery.[27–31] In the last two decades, different drug delivery methods have been developed to control drug dosage, target delivery and reduce the side effects. These methods can be classified as viral, chemical and physical.[31,33–37] Viral vectors are predominantly used for

[a]*Department of Engineering Design, Indian Institute of Technology Madras, India. E-mail: tuhin@iitm.ac.in; santra.tuhin@gmail.com; Tel: +91-44-2257-4747*
[b]*Department of Mechanical Engineering, Toyohashi University of Technology, Japan*
[c]*Department of Electrical Engineering, University of Cambridge, UK*
[d]*Department of Mechanical Engineering, Indian Institute of Technology Madras, India*

gene therapy; however, this technique is cell-specific and generates an immune response with high toxicity.[38] Chemical methods, such as basic protein and calcium phosphate, are frequently restricted by the low efficacy of plasmid delivery in various cell types due to their toxicity and plasmid degradation.[39] Different physical methods, such as jet injection, microinjection, mechanoporation, electroporation, photoporation, *etc.*, are being widely used for highly efficient cargo delivery with low toxicity.[40–49]

Physical approaches are widely being developed, which use physical energy to deform the cell plasma membrane and deliver cargo into cells.[27,31,35,50] For example, in electroporation, an electric field is required to deform cell membranes and create transient membrane pores for cargo delivery. However, it has limitations, such as electric field distortion, pH variation, sample contamination, and high toxicity effect, reducing cell viability.[41,42] The microinjection technique is time-consuming, and highly skilled technicians are required, which means delivery throughput is low, and therefore, microinjection not widely used.[27,28] The sonoporation method creates temporary membrane pores using shockwaves to carry biomolecules into cells. However, it produces high toxicity, and the substantial shear force easily causes cell damage and produces low cell viability.[51] On the other hand, photoporation technique involves light–matter interactions to disrupt the plasma membrane and deliver biomolecules into cells.[47,49] It is a contactless delivery technique, less invasiveness, less toxic for cells, and has been widely used in the past few years. However, its transfection efficacy in terms of different cell types and cell viability needs to be enhanced.

To address the various hurdles for cargo delivery into cells, we proposed a TiO_2 microspike-based photoporation platform to achieve highly controllable intracellular delivery with high delivery efficiency and cell viability. In this work, we fabricated microspikes on titanium substrate by electrochemical anodization process, and cells were cultured on them. Pulsed laser on the microspikes induces heat, resulting in cavitation bubble formation and jet flow on the cell membrane. Thus, the cell membrane creates transient membrane pores that allow delivery of molecules into cells with high efficiency and cell viability. Our TiO_2-based photoporation platform is flexible and highly effective for intracellular delivery, and it is appropriate for cellular therapy and diagnostics.

2. Materials and methods

2.1. Sample preparation

The titanium substrate was purchased from Sigma Aldrich, USA, with 0.25 mm sheet thickness. The sheet was cut to 20 × 20 mm in length and width. Afterward, the small sheets were etched with Kroll's reagent to eliminate the native oxides. Finally, they were ultrasonically cleaned using acetone and isopropyl alcohol (IPA), then dried under nitrogen.

2.2. Electrochemical anodization

TiO_2 microspikes were fabricated on a Ti (titanium) substrate using the electrochemical anodization technique. To fabricate microspikes, initially, Ti substrate was introduced into the beaker containing electrolyte, then a counter electrode was inserted with a fixed separation distance of 2 cm. A platinum electrode acted as a cathode, and Ti was used as anode. For Ti anodization, different voltages, time, and electrolyte compositions were used to fabricate the microspikes. The electrolyte was prepared by mixing 50 ml of 0.08 M hydrofluoric acid (HF) in 50 ml of 1 M sulfuric acid (H_2SO_4). The 100 ml electrolyte solution was continuously maintained, and the magnetic stirrer was rotated continuously at 300 rpm. The anodization voltage was varied from 0 to 40 V for 1 h with a DC power supply using ramp mode (2 V min^{-1}). The anodic current density was verified throughout the experimental process.[25] After fabrication, the sample was cleaned using a standard cleaning procedure with acetone, IPA (isopropyl alcohol), and deionized water, then dried by nitrogen gas. Finally, the cleaned sample was heated on a hot plate at 120 °C for five minutes.

2.3. Cell culture

For our photoporation experiment, human cervical cancer cells (HeLa) were used, purchased from the National Centre for Cell Science (NCCC), Pune, India. To culture HeLa cells, initially, the old medium was withdrawn from the cell culture dish using a pipette. Phosphate-Buffered Saline (PBS) was added into the cell culture dish, which was shaken in different orientations to properly clean the cell surface. The PBS cleaning procedure was carried out three times, and finally, it was completely removed from the dish surface. Afterward, 1 ml trypsin (0.05% trypsin–EDTA, GIBCO) was added to the cell culture dish. The culture was incubated for 5–7 minutes in an incubator at 37 °C in a 5% CO_2 atmosphere. As a result, cells were detached from the cell culture dish surface. Finally, 9 ml of DMEM (Dulbecco's Modified Eagle Medium, Thermo Fisher Scientific, USA, with 10% fetal bovine serum [FBS], Gibco, USA, and 1% penicillin–streptomycin) was added into the dish and mixed adequately with cells. The cells with DMEM medium were transferred on UV-treated microspike chip surface with a cell concentration of 1.2×10^6 cells per ml and incubated overnight in an incubator for the photoporation experiment.

2.4. Photoporation experimental procedure

After overnight cell culture, the HeLa cells have firmly adhered on the microspike chip surface. Then, we cleaned the cell surface using PBS, and the process was continuously repeated three times. Afterward, a fresh PBS solution with diluted PI dye was added into the chip surface with a PI dye concentration of 0.05 μl ml^{-1}. Then, the pulse laser was exposed and scanned on top of the chip surface. Photoporation experiments were carried out using Ekspla NT 342B-10-AW10 tunable nanosecond pulsed laser at 650 nm wavelength, with 5 ns pulse width and 10 Hz pulse frequency. For successful photoporation experiments, different pulse laser energies, PI dye concentrations, and laser scanning speeds were used to achieve highly efficient intracellular delivery with high cell viability.

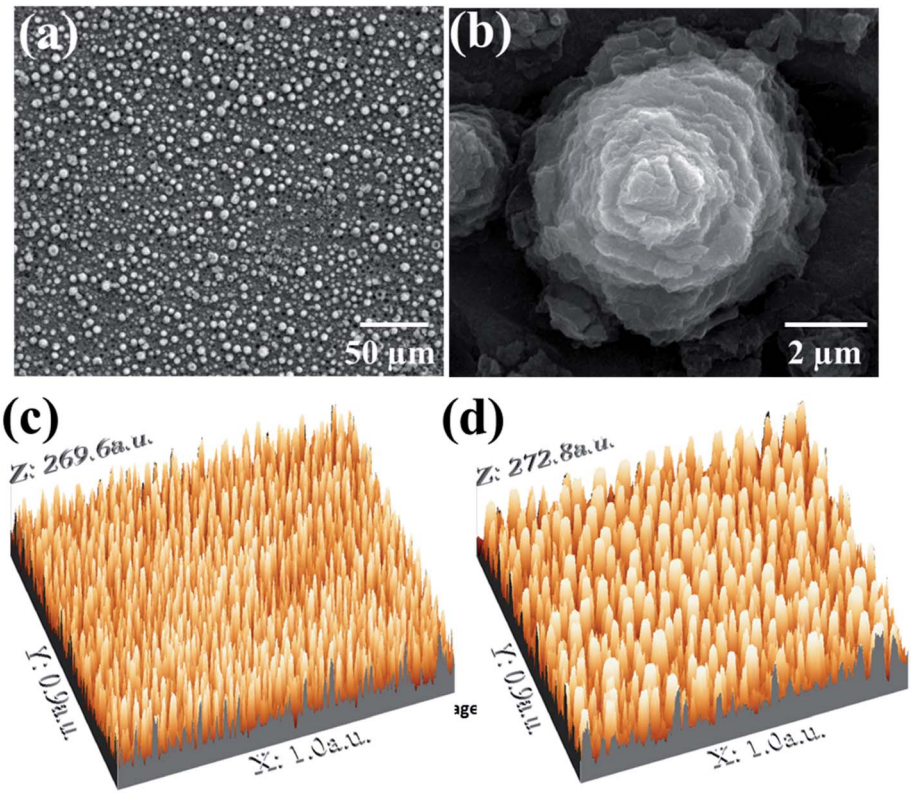

Fig. 1 The TiO_2 micro-spikes fabrication on Ti substrate using the electrochemical anodization process (a) the FESEM image of micro-spikes (b) single microspike at higher magnification (c and d) the 3D construction of micro-spikes from FESEM image at different magnifications.

2.5. Fluorescence microscopy

We used a non-inverted industrial fluorescence microscope (Nikon LV150N, Tokyo, Japan) with brightfield, darkfield, simple polarizing, double beam interferometry, and DIC attachments. To visualize fluorescence images, a 20× objective lens (NA/WD = 0.45/4.5 mm) was used, and a DS-Ri2 microscope CMOS camera (Nikon, 6fps [4908 × 3246 pixels] to 45 fps [1636 × 1088 pixels]) was used to capture the fluorescence images. Fluorescence excitation was provided by a 100 W mercury lamp. The excitation and emission of propidium iodide (PI) dye and calcein-AM were EX 535–550 nm/DM 575 nm/DM 580 nm and EX 470–540 nm/DM 505 nm/EM 510 nm.

2.6. Cell viability studies

Initially, PI dye delivery (red fluorescence) and calcein-AM stained live cells (green fluorescence) were recorded by a fluorescence microscope. Then, the images were analyzed using the Image J software.[52] The MTT (3-[4,5-dimethylthiazol-2-yl]-2,5-diphenyltetrazolium bromide, analytical grade, TCI, Japan) assay was accomplished using HeLa cells to measure the cell viability of all the tested samples, following the well-defined process in previous studies.[12,53] Each sample was added to a 30 mm cell culture plate, and HeLa cells were seeded with a density of 0.5×10^5 cells per mL. The MTT assay was performed after 2 h, 3 days, and 7 days before and after laser exposure of the samples. For the assay, 50 μl of 5 mg ml^{-1} MTT (stock) was added in each plate and then incubated at a temperature of 37 °C in a 5% CO_2 incubator for four hours, resulting in the formation of formazan crystals. Afterward, the cell culture medium containing MTT was removed from the culture plate by aspiration. Then, formazan crystals were dissolved by adding 500 μl dimethyl sulfoxide (DMSO, Sigma-Aldrich). Finally, 200 μl of dissolved formazan crystals with DMSO solution was transferred into a 96-well plate for the reading of optical density at 570 nm through a plate reader (AS ONE MPR-A 100).[54]

2.7. Characterization techniques

Attenuated total reflectance Fourier transform infrared spectra (ATR-FTIR) were recorded in the range of 400 to 4000 cm^{-1} using a Jasco FT/IR-6300 spectrometer to determine oxide formation on the microspike chip surface. Raman analyses were carried out using Jasco NRS-1000 laser Raman spectrophotometer with a 532 nm laser. The sample surface morphology was examined by a Quanta 400 field emission scanning electron microscope (FESEM) equipped with an Inca Penta Fetx3 (Oxford) energy-dispersive X-ray spectroscopy (EDS) analyzer for elemental analysis. The 3D profiles of FESEM images were obtained using the scanning probe image processor WSxM 7.0 software.[5] Water contact angles were measured using Surface Electro-Optics Phoenix contact angle meter through the sessile drop process. Water droplets of around ~8 μL were cautiously dropped onto the titanium and microspike surface using

a syringe. The contact angle was measured at different places on each sample, then the average value was reported. The composition of the samples was analyzed by X-ray photoelectron spectroscopy (XPS) using Quantera SXM-CI, scanning X-ray Microprobe, ULVAC-PHI, INC XPS system with 25 W, 15 kV non-monochromatic Al Kα radiation with 1486.6 eV energy. Core level spectra of Ti 2p, O 1s, and C 1s were obtained at the pass energy of 12.6 eV. The Ti 2p and O 1s core-level spectra were fitted with Gaussian–Lorentzian peaks to identify various species after subtracting a Shirley-type background using the CASAXPS software.[6] COMSOL multiphysics simulation software was used to calculate the spatial distribution of temperature.

3. Results and discussion

3.1. Morphology of microspikes

The surface morphology of the microspike device is shown in Fig. 1a. Fig. 1b shows the high-resolution FESEM image of a single microspike. 3D profiles of the FESEM images were acquired using the scanning probe image processor WSxM 7.0 software. Fig. 1c and d show the 3D images of the microspikes acquired from FESEM images. From these images, the high degree of arrangement of the microspike structure is confirmed. The height of microspikes is ~1.5 to 2 μm, with diameters of ~4 to 5 μm, and the average interspike spacing is ~8 to 10 μm. The wettability of the titanium substrate and microspikes was estimated using the water contact angle measurement. The water contact angle is ~66° on a bare titanium substrate, whereas water completely spreads on the microspike samples, confirming the super hydrophilicity.

3.2. TiO_2 microspike characterizations

3.2.1. ATR-FTIR analysis. The ATR-FTIR measurements were carried out in the range of 400–4000 cm^{-1} to define the oxide formation (Fig. 2a) on microspikes. The bands in the

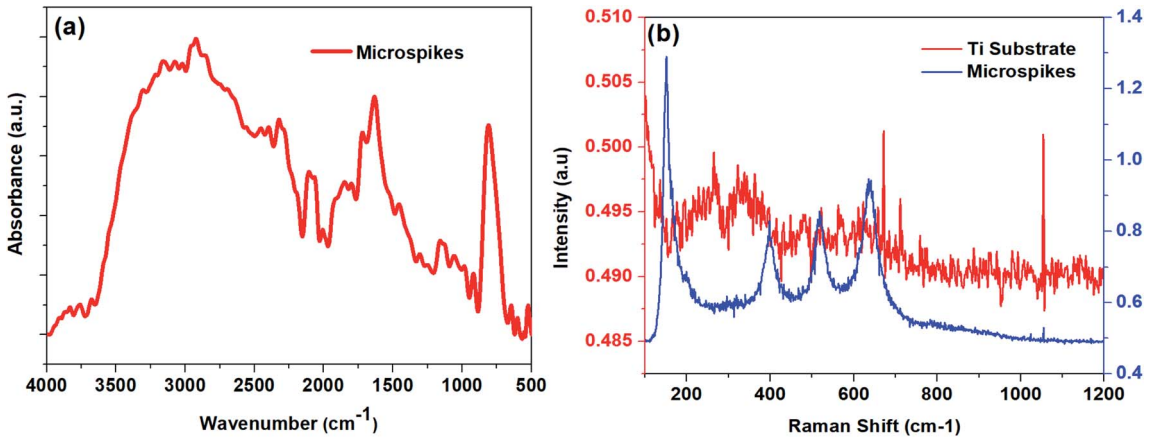

Fig. 2 (a) ATR-FTIR spectrum of micro-spikes (b) Raman spectra of micro-spikes and Ti substrate.

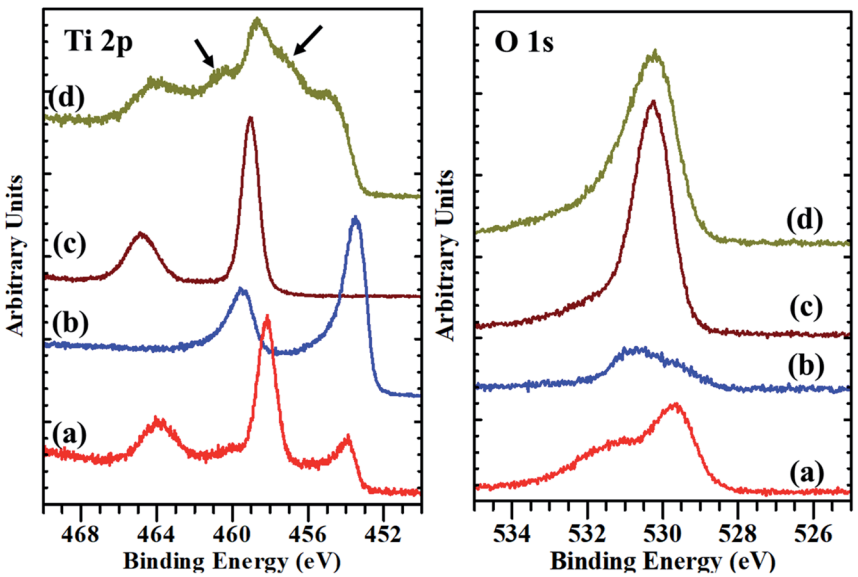

Fig. 3 The XPS core-level spectra of Ti 2p and O 1s: (a) substrate before etching, (b) substrate after etching, (c) micro-spikes before etching, (d) micro-spikes after etching.

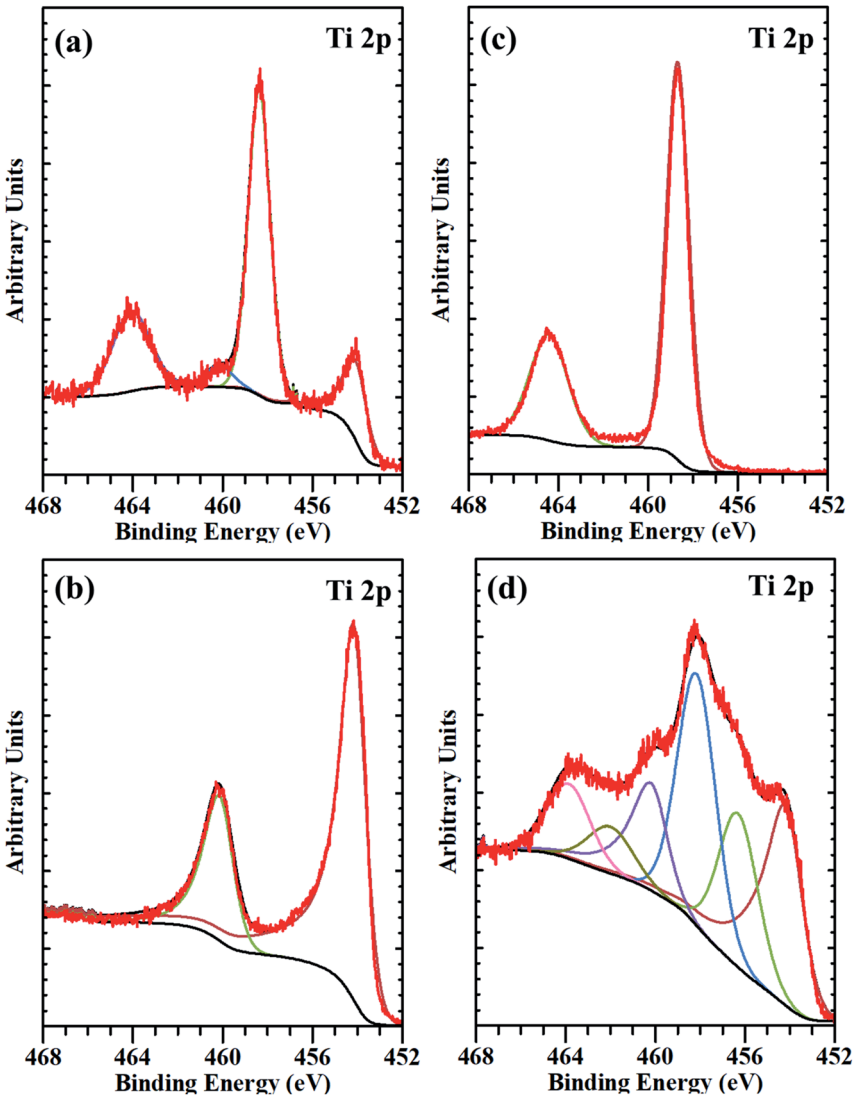

Fig. 4 The deconvoluted XPS spectra of Ti 2p core-level from (a) substrate before etching, (b) substrate after etching, (c) micro-spikes before etching, and (d) micro-spikes after etching.

range of 500–800 cm^{-1} could be due to the formation of Ti–O and Ti–O–Ti bonds, which originate from the oxide layer of the Ti_xO_y.[55,56] The peak from the 800 cm^{-1} to 900 cm^{-1} range is assigned to the formation of a O–O bond. The bands positioned at around 1620 to 1630 cm^{-1} and 3000 to 3350 cm^{-1} indicate the features of surface adsorbed hydroxyl groups and H_2O.[57,58]

3.2.2. Raman spectroscopy analysis. The Raman spectroscopy results (Fig. 2b) confirmed that the typical structures of titanium oxides are anatase and rutile in the tetragonal space group. The anatase structure has six Raman active modes, including $3E_g$, $2B_{1g}$, $1A_{1g}$, with Raman frequencies at 639 (E_g), 519 (B_{1g}), 513 (A_{1g}), 399 (B_{1g}), 197 (E_g), and 144 (E_g) cm^{-1}.[59–61] The rutile has four Raman active modes, B_{1g}, B_{2g}, E_g, and A_{1g}. The bulk Raman frequencies of the rutile phase are at 143 (B_{1g}), 447 (E_g), 612 (A_{1g}), and 826 (B_{1g}) cm^{-1}.[59] The existence of anatase and rutile peak shift from their positions, along with scattered Raman peaks, may be due to the abundant band structure.[61,62]

3.2.3. EDS and XPS analysis. The composition obtained using EDS on titanium substrate is 77.5 wt% Ti and 22.5 wt% oxygen. Microspikes have the elemental composition of 56.57 wt% oxygen and 43.43 wt% Ti. Furthermore, detailed XPS characterization has been carried out to understand the surface nature of the titanium substrate and microspikes. The Ti 2p and O 1s core-level spectra of Ti substrate and microspikes before and after etching were recorded and are presented in Fig. 3. The Ti 2p and O 1s core-level spectra from the substrate and microspike samples were fitted with Gaussian–Lorentzian peaks and are shown in Fig. 4 and Fig. 5, respectively. The bare Ti substrate shows several peaks indicating the presence of different Ti species, and they are resolved by curve fitting. The Ti $2p_{3/2}$ peaks at 454.1 and 458.4, along with spin–orbit peaks in the curve-fitted core-level spectrum, confirmed the presence of Ti metal and Ti^{4+} species in the substrate.[63,64] However, the relative concentration of TiO_2 species obtained from the area under the peak is much more than that of Ti metal in the

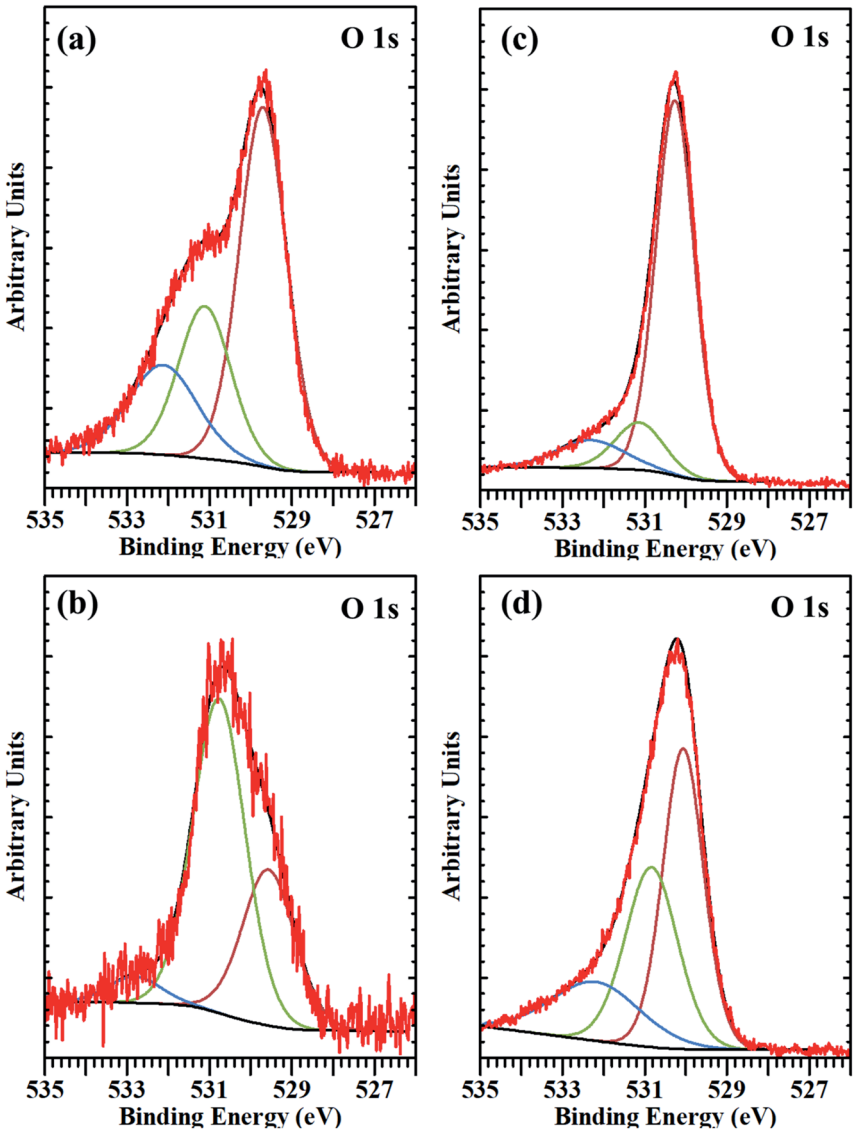

Fig. 5 The deconvoluted XPS spectra of O 1s core-level from (a) substrate before etching, (b) substrate after etching, (c) micro-spikes before etching, and (d) microspikes after etching.

substrate, indicating surface oxidation of the Ti substrate (Fig. 4a). The mild sputter etching of the substrate shows only Ti metal peaks ($2p_{3/2}$ at 454.2 eV), as presented in Fig. 4b. The Ti $2p_{3/2,1/2}$ peaks at 458.7 and 464.4 eV in microspikes indicate the presence of TiO_2 species, which is clear from its Ti 2p core-level spectrum (Fig. 4c). The Ti 2p core-level spectrum of microspikes after sputter etching is broad in nature, containing several Ti species, and is decomposed into component peaks by curve-fitting, as displayed in Fig. 4d. The decomposed Ti $2p_{3/2}$ peaks observed at 454.2, 456.3, and 458.1 eV are assigned to Ti metal, Ti sub-oxide (Ti_xO_y/defects), and TiO_2 species, respectively.[63,65–68] The relative concentration of the TiO_2 is the dominating one among all the Ti species. It is important to note that an intermediate sub-oxide species was observed around 456.3 eV, which could be due to defect formation.[66–69] The surface concentrations, binding energies of the Ti substrate, and microspike component species evaluated from XPS studies are shown in Tables 1 and 2. The O 1s core levels of Ti substrate

Table 1 Composition of substrate and microspike samples obtained from XPS

Sample/species	Titanium substrate before etching (at%)	Titanium substrate after etching (at%)	Microspikes before etching (at%)	Microspikes after etching (at%)
Ti 2p	20.7	65.6	31.5	32.1
O 1s	79.3	34.4	68.5	67.9

Table 2 Binding energy of Ti 2p and O 1s core levels in different compounds with relative peak area percentage

Sample	Ti species	Ti $2p_{3/2}$ binding energy (eV)	Relative peak area (%)	O species	O binding energy (eV)	Relative peak area (%)
Ti substrate before etching	Ti^0	454.1	20.5	Oxide	530.0	54.6
	Ti^{4+}	458.4	79.5	OH^-	531.1	25.7
				Adsorbed H_2O	532.1	19.7
Ti substrate after etching	Ti^0	454.2	100	Oxide	530.0	31.4
				OH^-	530.8	63.3
				Adsorbed H_2O	532.8	5.3
Microspikes before etching	Ti^{4+}	458.7	100	Oxide	530.3	77.3
				OH^-	531.1	12.4
				Adsorbed H_2O	532.3	10.3
Microspikes after etching	Ti^0	454.2	30	Oxide	530.1	44.4
	Ti_xO_y (Ti^{3+}/Ti^{2+})	456.3	27	OH^-/defects	531.5	35.1
	Ti^{4+}	458.2	43	Adsorbed H_2O	532.2	19.5

and of the microspikes before and after etching conditions were also recorded and are shown in Fig. 5. The broad nature of their spectra suggests the existence of different oxygen species present on their surface, and the spectra can be curve-fitted into several components of oxygen species.[65] An intense peak around 530 eV is ascribed to oxide species present in the substrate and microspikes at different conditions. The observed peaks around 531 eV and >532.5 eV correspond to oxygen adsorbed on the surface or are related to the hydroxyl (OH^-) species and surface-adsorbed H_2O.[6,65] In the case of microspike O 1s after sputter etching, the peak around 531.5 eV could correspond to Ti_xO_y (may overlap with OH^-), which is due to the oxygen vacancies (defective oxides).[67] The O 1s component (defects and OH^-) peaks' area under the curve (AUC) was measured and is presented in Fig. 6a. The increase in the AUC of Ti_xO_y after etching microspike samples confirms the oxygen defects (Ti_xO_y) on microspikes. Similarly, the AUC of the microspike Ti 2p (from Fig. 4d) is presented in Fig. 6b. This substantiates the presence of Ti and Ti_xO_y, along with TiO_2. The corresponding defect oxide peaks are also observed in the microspike Ti 2p spectrum after etching (Fig. 3d, 4d, and 5d).

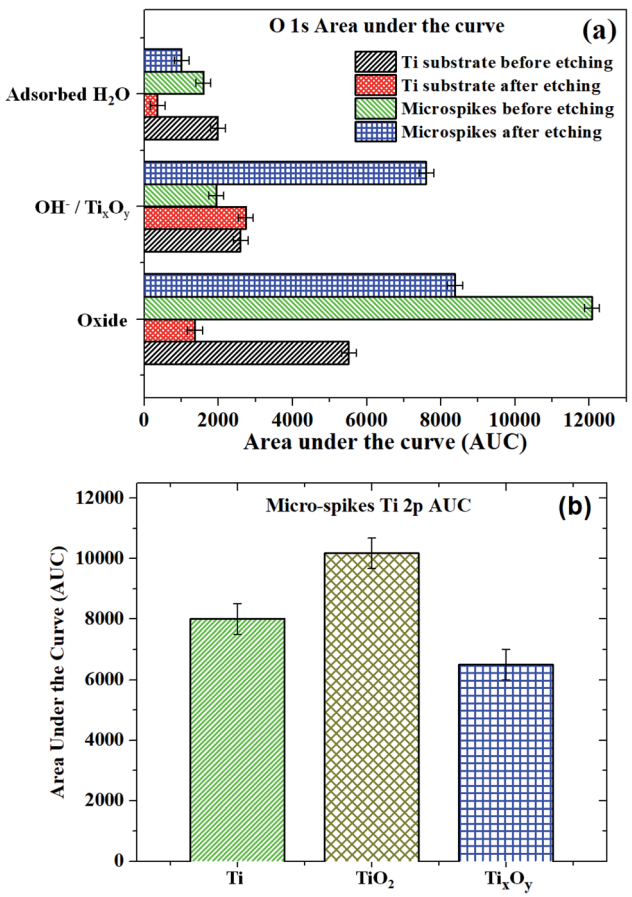

Fig. 6 Area under the curve (AUC) obtained from components peaks of (a) O 1s and (b) Ti 2p of micro-spikes after etching.

3.3. Theoretical study

To unveil the causes of intracellular delivery in microspikes structures, we performed Comsol Multiphysics simulations of electromagnetic radiation in the mixed titanium oxide structures. To reduce the mesh size, we simplified the complex structure of microspikes consisting of a 2 μm wide TiO_2 (anatase phase is considered here) rectangular microsubstrate, which emerged in a water environment. The surface of this substrate is decorated with semi-circular Ti_3O_5 structures. Here, we have considered Ti_3O_5 as the dominant suboxide of Ti species, as seen in the peak at ~456.3 eV in XPS spectra (Fig. 3d).[70] Since the shape and size distributions of these Ti_3O_5 structures are unknown, we have taken the arbitrary diameter of around 400 nm in the model. To simulated resistive heating due to pulsed laser exposure with the fluence of 35 mJ cm^{-2} (5 ns pulse duration), we used the emw module of Comsol Multiphysics. In the simulation, values of refractive indices are $n = 3.2 + i1.8$ for Ti_3O_5,[71] $n = 2.55$ for TiO_2 and $n = 1.33$ for water. The spatial distribution of resistive heating, as shown in Fig. 7a, clearly shows that the heating effect is localized into the Ti_3O_5 structures, which act as heat sources due to pulsed laser exposure. To probe the temporal and spatial distribution of temperatures, the following transient model has been adapted:

$$C_l \frac{\partial T_l}{\partial t} = \nabla(k_l \nabla T_l) - g_{lw}(T_l - T_w) - g_{ls}(T_l - T_n) + Q(t) \quad (1)$$

$$\rho_s C_s \frac{\partial T_s}{\partial t} = \nabla(k_s \nabla T_s) + g_{ls}(T_l - T_s) - g_{sw}(T_s - T_w) \quad (2)$$

$$\rho_w C_w \frac{\partial T_w}{\partial t} = \nabla(k_w \nabla T_w) + g_{lw}(T_l - T_w) + g_{sw}(T_s - T_w) \quad (3)$$

Here, T_l is the lattice temperature of Ti_3O_5, T_s is the temperature of TiO_2 micro-substrate and T_w is water temperature. $Q(t)$ is the transient heat due to pulsed laser irradiation. $g_{ab}(T_a - T_b)$ is the heat transfer from medium a to b, with g_{ab} being the boundary interface heat exchange with the Ti_3O_5/water interface, $g_{lw} = 28 \times 10^8$ W m^{-2} K^{-1}; Ti/TiO_2 interface $g_{ls} = 28 \times 10^8$ W m^{-2} K^{-1}; and TiO_2/water interface $g_{sw} = 31 \times 10^8$ W m^{-2} K^{-1}, calculated following ref. 72. $k_l = 0.4$ W m^{-1} K^{-1} is the thermal conductivity of lattice and $C_l = 3.6 \times 10^6$ J m^{-3} K^{-1} is the lattice specific heat of Ti_3O_5.[73] $C_w = 4182$ J kg^{-1} K^{-1} and $C_s = 938$ J kg^{-1} K^{-1} are the heat capacities of water and TiO_2 substrate (obtained from Dulong Petit law), respectively. The mass density is $\rho_w = 1000$ kg m^{-3} of water and $\rho_n = 4260$ kg m^{-3} of TiO_2, respectively. The transient temperatures T_l and T_w are shown in Fig. 7b for an arbitrary point on the Ti_3O_5/water interface. The temperature distribution in the model at the peak of temperature transient is shown in Fig. 7c and d at 23 ns and 100 ns, respectively. It is shown that the temperature diffuses from the Ti_3O_5 structures to the surrounding environments after pulse laser exposure. The temperature rise is significantly high enough (>550 K) to induce cavitation bubbles at the Ti_3O_5/water interface.[50,74] These bubbles were generated, expanded, and destroyed, eventually resulting in strong jet flow in the vicinity of the cell membrane. As a result, the cell membranes deformed, generating transient pores which allow extracellular molecules to diffuse into the cell cytosol. It is worth mentioning that we did not include any phase transitions induced by the temperature rise of the materials in the simulation. Also, note that the heating effect would be different for different shapes and sizes of materials. This model is just presented to establish the fact that the

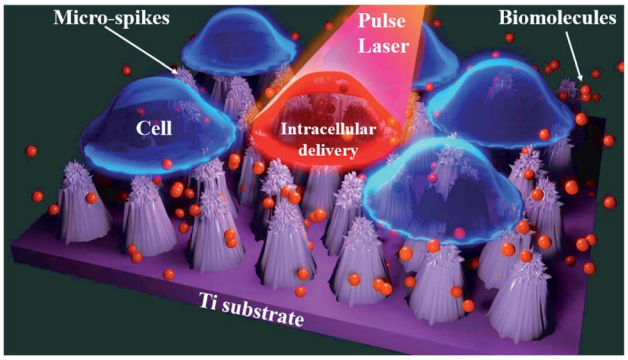

Fig. 8 The schematic of pulse laser-assisted intracellular delivery using micro-spikes. Due to pulse laser interaction with micro-spikes, it heats up and induce cavitation bubbles resulting strong fluid flow at cell membrane surface. Thus, cell membrane can deform and create transient membrane pores and delivery molecules into cells.

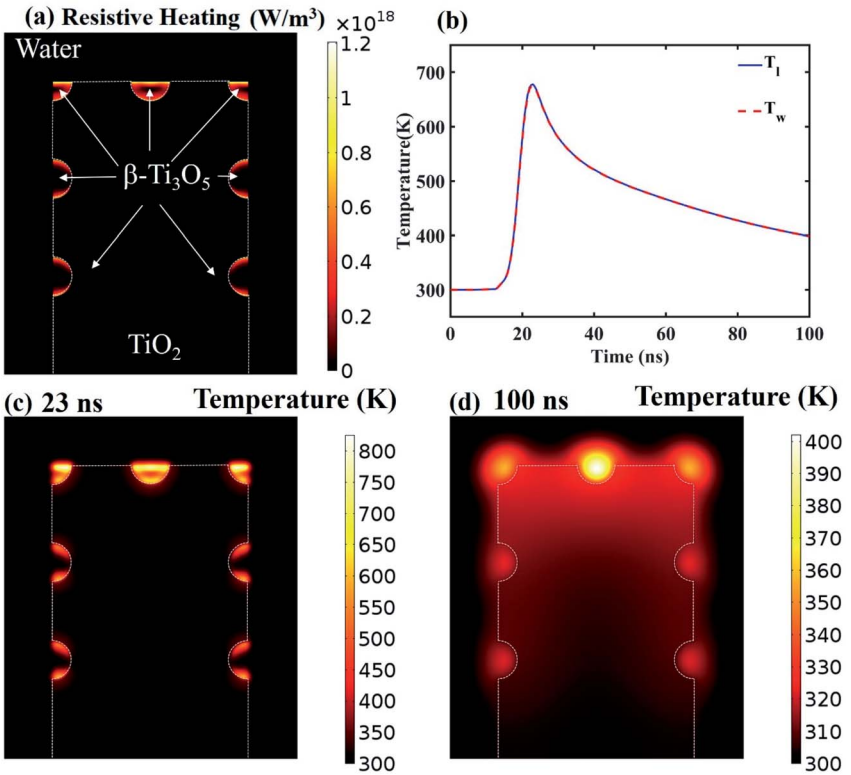

Fig. 7 (a) Spatial distribution of resistive heating in the model structure. (b) Temporal heating and cooling at an arbitrary point of β-Ti_3O_5/water interface. (c) Spatial distribution of the temperatures at 23 ns (the peak position of the transient in (b)). (d) Spatial distribution of the temperatures at 100 ns of the transient.

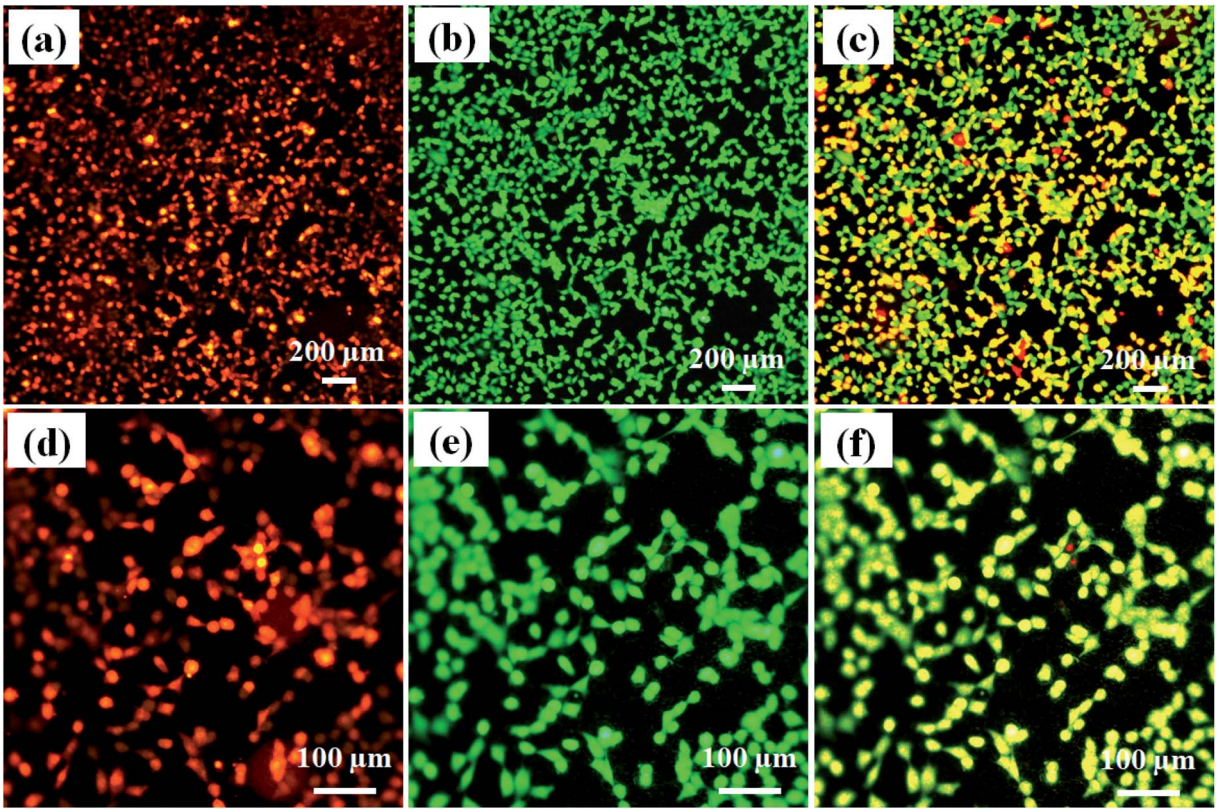

Fig. 9 PI dye delivery and cell viability (a) PI dye delivery in HeLa cells (b) cell viability using calcein AM (c) merge image. (d–f) at higher magnification.

heating effect plays an important role in intracellular delivery in the microspike platform.

3.4. Laser exposure on microspike device

3.4.1. Intracellular delivery. Photoporation experiments were carried out using a tunable nanosecond pulse laser. After performing the cell culture overnight on a microspike device, the culture was cleaned by PBS and PI dye was added to the device surface, and then it was exposed to a pulse laser. The PI dye is cell impermeable, and it cannot enter inside live cells until the membrane ruptures and creates transient membrane nanopores. The dye only can enter due to cell membrane deformation and produce red fluorescence color in the cell cytosol by a simple diffusion process.[47,75]

Fig. 8 shows the schematic of pulse laser-assisted intracellular delivery using the microspike device. Due to pulse laser exposure on the microspike device, the microspikes heat up, resulting in vaporization of surrounding cell medium and the creation of cavitation bubbles. These cavitation bubbles can rapidly grow, coalesce and collapse, resulting in steady fluid flow on the microspikes–cell membrane interface. As a result, the cell membrane deformed and created transient hydrophilic nanopores, which allowed PI molecules to diffuse inside cells. After laser exposure with PI molecules, the microspike device surface was washed with PBS, and calcein-AM was added to the device and incubated for ten minutes. Calcein-AM is a cell-permeable dye, and it can cause hydrolysis inside live cells, thus producing green fluorescence.[47,75]

Fig. 9a shows the PI dye delivery in HeLa cells using 7 mJ laser fluence at 650 nm wavelength, with 5 ns pulse width and 10 Hz pulse frequency. The red fluorescence image of the figure confirms that PI dye is delivered successfully into the HeLa cells. Fig. 9b shows calcein-AM imaging, where most of the cells are live after delivery. Fig. 9c shows the merged image of PI dye delivery and calcein-AM imaging, which also confirmed that most of the cells are live, with green and yellowish-green fluorescence. Fig. 9d–f show the same at higher magnification on different laser exposure areas of the device.

3.4.2. Delivery efficiency and cell viability. The delivery efficiency and cell viability reached approximately 93% and 98%, as shown in Fig. 10a. For the delivery efficiency calculation, we counted the number of fluorescent cells delivered PI dye (Fig. 10a), divided by the total number of cells and multiplied by 100%. To calculate cell viability, the same procedure was followed after calcein-AM staining and imaging (Fig. 10b).

Moreover, the 3-(4,5-dimethylthiazol-2-yl)-2,5-diphenyltetrazolium bromide assay was used to identify cell viability after laser exposure on microspikes with HeLa cells. To check the device biocompatibility, we also compared the microspikes device's cell viability and proliferation efficiency without laser exposure. The MTT experiments were conducted for 2 h, 3 days and 7 days on all samples to inspect cell proliferation and cell viability. Substantial improvement of viable

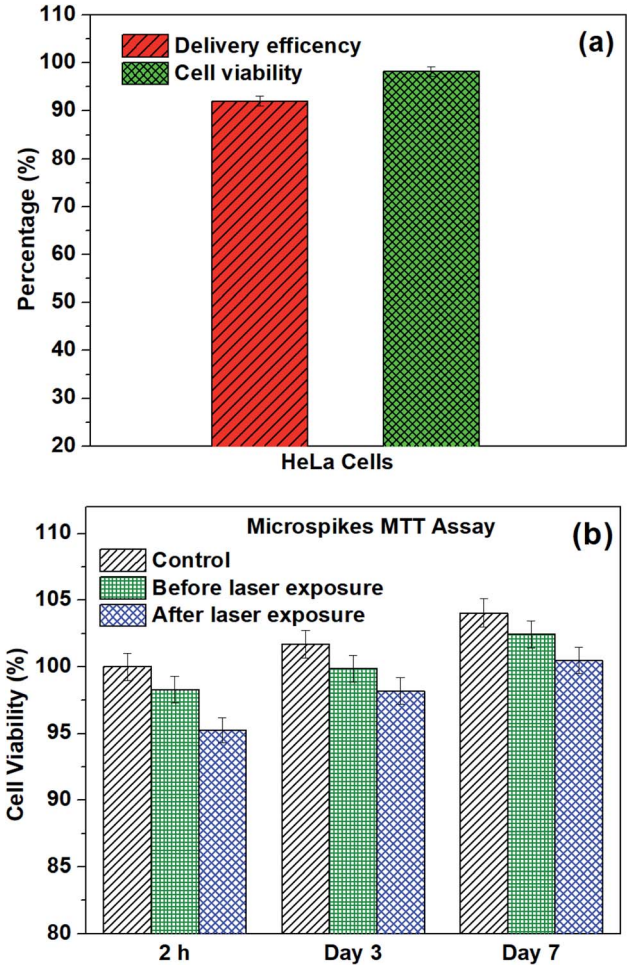

Fig. 10 (a) Delivery efficiency and cell viability on microspikes using image analysis and (b) cell viability of HeLa cells using MTT assay on different days before and after laser exposure on micro-spikes.

cells adhering on the chip surface before and after laser exposure was reflected in the increased absorbance at an optical density (OD) of 570 nm after 3 and 7 days incubation. The absorbance values were converted into the percentage of cell viability, as shown in Fig. 10b. After 2 h of laser exposure (microspikes), the cell viability is ~95.25% ± 0.95, which is ~3% deviated from the microspike device (without laser exposure), *viz* ~98.30% ± 0.98 and 5% deviation for cells only (without the device). These results also substantiate the cell viability results obtained using fluorescence images (Fig. 10a). The numbers of viable cells on microspikes further increase after incubation for 3 days (~99.8 ± 0.99 before and 98.2% ± 0.98 after laser exposure). No apparent cytotoxicity was observed even after longer incubation (7 days). These results suggest that the fabricated device (microspikes) does not show significant cytotoxicity. However, after laser exposure, about ~3% cell death was observed. Conversely, the number of cells and proliferation efficiency increases after incubation for 3 and 7 days. The fluorescence microscopy images confirmed the attachment of HeLa cells after laser exposure on samples. The cells have well-spread morphology, representing that they are firmly attached to the surface of the microspikes. Cell growth increases with an increase in the incubation time.

3.5. Laser exposure on a bare titanium substrate (without microspikes)

The experiments were performed on titanium substrate (without microspikes) to cross-check the delivery efficiency/mechanism. Fig. 11a shows the PI dye-stained nuclei of dead cells due to laser exposure (same parameters of microspikes) on the titanium substrate. Fig. 11b shows calcein-AM stained live cells after laser exposure. Cell viability was calculated using image analysis and MTT assay before and after laser exposure on titanium substrate, as shown in Fig. 12. These results clearly show that no PI dye delivery took place in the absence of microspikes, strongly validating that PI dye delivery into cells is mainly because of the laser and microspike interaction-based photoporation or optoporation mechanism.

3.6. Intracellular delivery mechanism on microspikes

We hypothesize the possible photoporation mechanism of intracellular delivery using microspikes as follows. The PI dye is

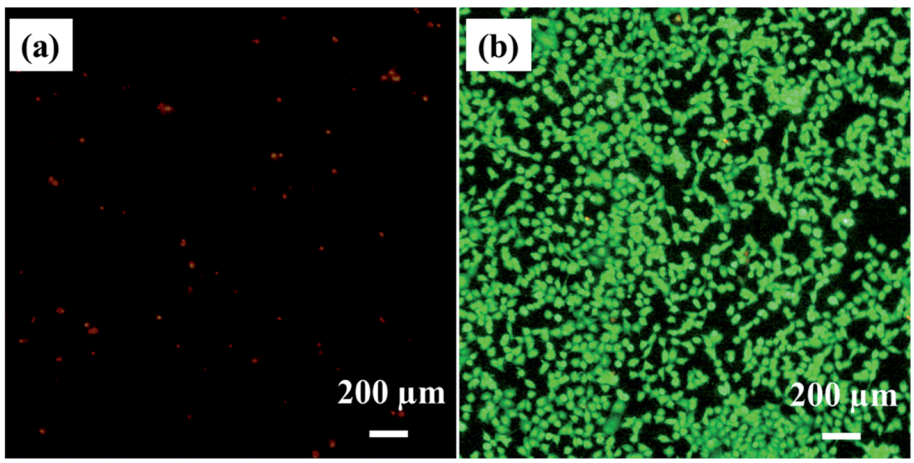

Fig. 11 Laser exposure on titanium substrate (without micro-spikes) (a) PI dye staining on the nucleus of dead cells (b) cell viability test using calcein-AM confirmed that most of the cells are live (green color).

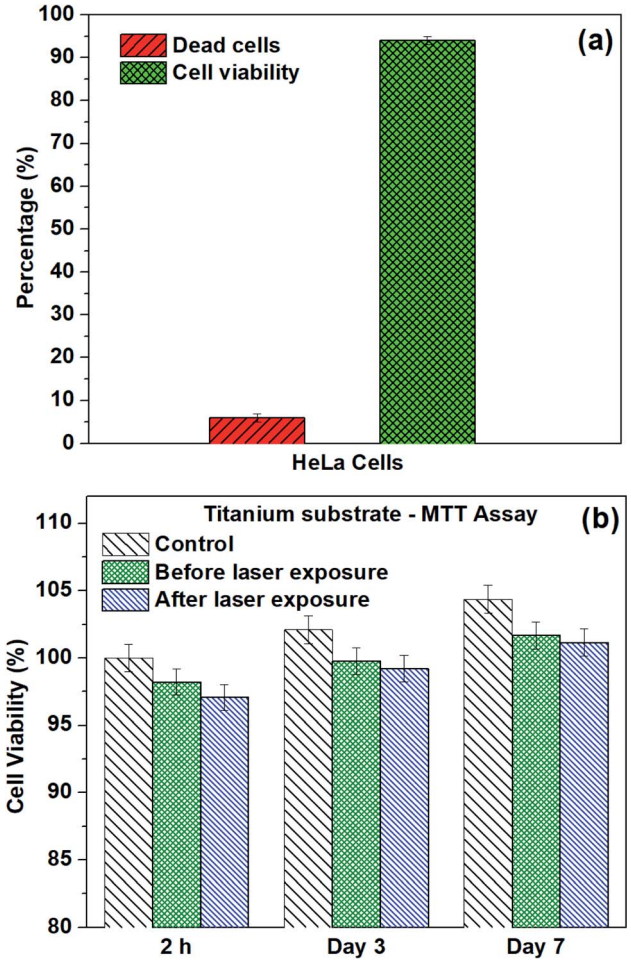

Fig. 12 (a) Dead cells and viable cells after laser exposure on titanium substrate using image analysis and (b) cell viability of HeLa cells using MTT assay on different days before and after laser exposure on titanium substrate (without microspikes).

cell impermeable; it can only enter the cell and produce red fluorescence color if any mechanical membrane rupture forms by application of some external energy to create transient membrane pores. Due to pulse laser exposure on the microspike device, the microspikes heated up, vaporizing the surrounding cell medium and creating cavitation bubbles. These laser-induced cavitation bubbles rapidly grow and burst, resulting in steady fluid flow on the TiO_2 microspike–cell membrane interface. As a result, the cell membrane deformed and created temporary hydrophilic nanopores, which allowed PI molecules to diffuse inside the cells.

The core-level spectra of Ti 2p and O 1s were studied by X-ray photoelectron spectroscopy (XPS). The Ti 2p spectrum of the microspike samples shows that it has Ti^0, Ti^{2+}/Ti^{3+}, and Ti^{4+}. Simultaneously, the O 1s spectrum validates the high concentration of oxygen vacancy defects in these samples' lattice. These defects are initiated by the Ti^{3+} unsaturated coordination, forming the basis for more free electrons. The oxygen defects have quasi-metallic and metallic properties, even though they are semiconducting. Atmospheric contamination shows oxides that are a few Å to nm thick, whereas the interaction between the laser and microspikes is perhaps at a few nm depth. The Ti^0, Ti^{2+}/Ti^{3+}, and Ti^{4+} (on microspikes) below the oxide layer probably interact with irradiated nanosecond pulse laser to cause the laser-induced cavitational bubbles, which disrupt the cell membrane for intracellular delivery; this is not possible on the pristine titanium substrate.

The oxide formed by electrochemical anodization may be deficient in oxygen, which leads to the formation of a mixed oxide. XPS analysis indicates that the formed oxide layer mostly contains TiO_2, Ti_xO_y, and Ti, where the Ti_xO_y may have quasi-metallic and the Ti metallic properties. The formed Ti_3O_5 and Ti_xO_y have quasi-metallic properties and exhibit absorbance in the green to red region. These oxides may photothermally create heat, PNBs, cavitational bubbles, and/or reactive oxygen species (ROS), which aid in creating resealable pores on the cells for entry of PI from the outside to the inside of the cells.[76] However, the exact mechanism for intracellular delivery by the microspike-based photoporation is uncertain. It can be understood that intracellular delivery may occur due to the combination of the mechanisms stated above.

4. Conclusions

In summary, microspikes have been fabricated on titanium substrate using an electrochemical anodization process. The interaction between laser and microspikes induced cavitation bubbles, which rapidly grow, coalesce, and collapse. As a result, a strong fluid flow is generated at the microspike and cell membrane interface, which disrupts the plasma membrane and creates transient membrane pores for highly efficient intracellular delivery into the cell. We successfully delivered propidium iodide dye into HeLa cells with high delivery efficiency and high cell viability. Thus, our platform can perform highly efficient intracellular drug delivery and shows potential applicability in cellular therapy and diagnostics.

Conflicts of interest

The authors declare no conflict of interest.

Acknowledgements

We greatly appreciate the financial support from the DBT/Wellcome Trust India Alliance Fellowship under grant number IA/E/16 1 503062 and the Indian Institute of Technology Madras Exploratory research grant ED1920904RFER008754. The authors would like to thank Dr Parthasarathi Bera, Surface Engineering Division, CSIR-National Aerospace Laboratories, India, for discussion on the XPS analysis. The authors would like to thank Dr Pallavi Gupta and Ms. B. Nandhini for their help. XPS measurements were carried out using a Quantera SXM-CI, scanning X-ray Microprobe, ULVAC-PHI, INC XPS system in the Cooperative Research Facility Center at the Toyohashi University of Technology. Help from Mr Saitou Toshihide, CRFC, Toyohashi University of Technology,

Japan, for XPS studies is gratefully acknowledged. The author would like to thank SAIF, IITM, for the FESEM and EDS studies.

References

1 M. Kaur and K. Singh, *Mater. Sci. Eng., C*, 2019, **102**, 844–862.
2 L. Mohan, D. Durgalakshmi, M. Geetha, T. S. N. S. Narayanan and R. Asokamani, *Ceram. Int.*, 2012, **38**, 3435–3443.
3 D. Regonini, C. R. Bowen, A. Jaroenworaluck and R. Stevens, *Mater. Sci. Eng., R*, 2013, **74**, 377–406.
4 K. Kalantar-zadeh, A. Z. Sadek, H. Zheng, J. G. Partridge, D. G. McCulloch, Y. X. Li, X. F. Yu and W. Wlodarski, *Appl. Surf. Sci.*, 2009, **256**, 120–123.
5 L. Mohan, C. Anandan and N. Rajendran, *Mater. Sci. Eng., C*, 2015, **50**, 394–401.
6 C. Anandan, L. Mohan and P. D. Babu, *Appl. Surf. Sci.*, 2014, **296**, 86–94.
7 L. Mohan, C. Anandan and N. Rajendran, *Electrochim. Acta*, 2015, **155**, 411–420.
8 L. Mohan, C. Anandan and N. Rajendran, *RSC Adv.*, 2015, **5**, 41763–41771.
9 M. Ghorbani, F. Nasirpouri, A. Iraji zad and A. Saedi, *Mater. Des.*, 2006, **27**, 983–988.
10 H. E. Prakasam, O. K. Varghese, M. Paulose, G. K. Mor and C. A. Grimes, *Nanotechnology*, 2006, **17**, 4285–4291.
11 H. Tsuchiya and P. Schmuki, *Electrochem. Commun.*, 2005, **7**, 49–52.
12 L. Mohan, S. Kar, B. Nandhini, S. S. Dhilip Kumar, M. Nagai and T. S. Santra, *Mater. Today Commun.*, 2020, 101403.
13 R. L. Karlinsey, *Electrochem. Commun.*, 2005, **7**, 1190–1194.
14 Y. F. Yuan, X. H. Xia, J. B. Wu, J. L. Yang, Y. B. Chen and S. Y. Guo, *Electrochem. Commun.*, 2010, **12**, 890–893.
15 V. D. Patake and C. D. Lokhande, *Appl. Surf. Sci.*, 2008, **254**, 2820–2824.
16 E. Reimhult, K. Kumar and W. Knoll, *Nanotechnology*, 2007, **18**, 275303.
17 N. R. de Tacconi, C. R. Chenthamarakshan, G. Yogeeswaran, A. Watcharenwong, R. S. de Zoysa, N. A. Basit and K. Rajeshwar, *J. Phys. Chem. B*, 2006, **110**, 25347–25355.
18 K. Kalantar-zadeh, A. Z. Sadek, J. G. Partridge, D. G. McCulloch, Y. X. Li, X. F. Yu, P. G. Spizzirri and W. Wlodarski, *Thin Solid Films*, 2009, **518**, 1180–1184.
19 K. Indira, S. Ningshen, U. K. Mudali and N. Rajendran, *Mater. Charact.*, 2012, **71**, 58–65.
20 K. Indira, U. K. Mudali and N. Rajendran, *Ceram. Int.*, 2013, **39**, 959–967.
21 L. Mohan, S. Viswanathan, C. Anandan and N. Rajendran, *RSC Adv.*, 2015, **5**, 93131–93138.
22 S. Viswanathan, L. Mohan, S. John, P. Bera and C. Anandan, *Surf. Interface Anal.*, 2017, **49**, 450–456.
23 S. Viswanathan, L. Mohan, P. Bera and C. Anandan, *RSC Adv.*, 2016, **6**, 74493–74499.
24 H. Wu, Y. Wang, Y. Ma, T. Xiao, D. Yuan and Z. Zhang, *Ceram. Int.*, 2015, **41**, 2527–2532.
25 L. Mohan, C. Dennis, N. Padmapriya, C. Anandan and N. Rajendran, *Mater. Today Commun.*, 2020, 101103.
26 M. Supernak-Marczewska, A. Ossowska, P. Strąkowska and A. Zieliński, *Adv. Mater. Sci.*, 2018, **18**, 17–23.
27 *Essentials of single-cell analysis: concepts, applications and future prospects*, ed. F.-G. Tseng and T. S. Santra, Springer, 2016.
28 T. S. Santra and F.-G. Tseng, *Handbook of Single-cell Technologies*, Springer Verlag, Singapore, 2021.
29 D. W. Pack, A. S. Hoffman, S. Pun and P. S. Stayton, *Nat. Rev. Drug Discovery*, 2005, **4**, 581–593.
30 Z. Gu, A. Biswas, M. Zhao and Y. Tang, *Chem. Soc. Rev.*, 2011, **40**, 3638–3655.
31 P. Shinde, A. Kumar, K. Illath, K. Dey, L. Mohan, S. Kar, T. K. Barik, J. Sharifi-Rad, M. Nagai and T. S. Santra, in *Delivery of Drugs*, Elsevier, 2020, pp. 161–190.
32 J. Li and K. Kataoka, *J. Am. Chem. Soc.*, 2021, **143**(2), 538–559.
33 S. Nayak and R. W. Herzog, *Gene Ther.*, 2010, **17**, 295–304.
34 R. M. Schmid, H. Weidenbach, G. F. Draenert, S. Liptay, H. Lührs and G. Adler, *Gut*, 1997, **41**, 549–556.
35 S. Lakshmanan, G. K. Gupta, P. Avci, R. Chandran, M. Sadasivam, A. E. S. Jorge and M. R. Hamblin, *Adv. Drug Delivery Rev.*, 2014, **71**, 98–114.
36 P. Shinde, L. Mohan, A. Kumar, K. Dey, A. Maddi, A. N. Patananan, F. G. Tseng, H. Y. Chang, M. Nagai and T. S. Santra, *Int. J. Mol. Sci.*, 2018, **19**(10), 3143.
37 A. Kumar, L. Mohan, P. Shinde, H.-Y. Chang, M. Nagai and T. S. Santra, in *Handbook of Single Cell Technologies*, Springer, Singapore, 2018, pp. 1–29.
38 Z. C. Hartman, D. M. Appledorn and A. Amalfitano, *Virus Res.*, 2008, **132**, 1–14.
39 R. G. Crystal, *Science*, 1995, **270**, 404–410.
40 M. R. Capecchi, *Cell*, 1980, **22**, 479–488.
41 T. S. Santra and F. G. Tseng, *Micromachines*, 2013, **4**, 333–356.
42 S. Kar, L. Mohan, K. Dey, P. Shinde, H.-Y. Chang, M. Nagai and T. S. Santra, *J. Micromech. Microeng.*, 2018, **28**, 123002.
43 D. H. Fuller, P. Loudon and C. Schmaljohn, *Methods*, 2006, **40**, 86–97.
44 S. Ohta, K. Suzuki, Y. Ogino, S. Miyagawa, A. Murashima, D. Matsumaru and G. Yamada, *Dev., Growth Differ.*, 2008, **50**, 517–520.
45 A. Sharei, J. Zoldan, A. Adamo, W. Y. Sim, N. Cho, E. Jackson, S. Mao, S. Schneider, M.-J. Han, A. Lytton-Jean, P. A. Basto, S. Jhunjhunwala, J. Lee, D. A. Heller, J. W. Kang, G. C. Hartoularos, K.-S. Kim, D. G. Anderson, R. Langer and K. F. Jensen, *Proc. Natl. Acad. Sci. U. S. A.*, 2013, **110**, 2082–2087.
46 M. Hima, G. Pallavi, L. Mohan, M. Nagai, S. Wankhar and T. S. Santra, in *Microfluidics and Bio-MEMS Devices and Applications*, ed. T. S. Santra, Jenny Stanford Publisher Pvt. Ltd., Singapore, 2020, p. 68.
47 T. S. Santra, S. Kar, C.-W. Chen, J. Borana, T.-C. Chen, M.-C. Lee and F.-G. Tseng, *Nanoscale*, 2020, **12**, 12057.
48 T. S. Santra, P.-C. Wang, H.-Y. Chang and F.-G. Tseng, *Appl. Phys. Lett.*, 2013, **103**, 233701.
49 T. S. Santra, S. Kar, H.-Y. Chang and F.-G. Tseng, *Lab Chip*, 2020, **20**, 4194–4204.

50 P. Shinde, S. Kar, L. Mohan, H.-Y. Chang, F.-G. Tseng, M. Nagai and T. S. Santra, *ACS Biomater. Sci. Eng.*, 2020, **6**(10), 5645–5652.
51 I. Lentacker, I. De Cock, R. Deckers, S. C. De Smedt and C. T. W. Moonen, *Adv. Drug Delivery Rev.*, 2014, **72**, 49–64.
52 I. Horcas, R. Fernández, J. M. Gomez-Rodriguez, J. Colchero, J. Gómez-Herrero and A. M. Baro, *Rev. Sci. Instrum.*, 2007, **78**, 13705.
53 L. Mohan, M. Chakraborty, S. Viswanathan, C. Mandal, P. Bera, S. T. Aruna and C. Anandan, *Surf. Interface Anal.*, 2017, **49**(9), 828–836.
54 L. Mohan, M. D. Raja, T. S. Uma, N. Rajendran and C. Anandan, *J. Mater. Eng. Perform.*, 2016, **25**, 1508–1514.
55 N. Liu, X. Chen, J. Zhang and J. W. Schwank, *Catal. Today*, 2014, **225**, 34–51.
56 Q. Chen, G. H. Du, S. Zhang and L.-M. Peng, *Acta Crystallogr., Sect. B: Struct. Sci.*, 2002, **58**, 587–593.
57 T. Gao, H. Fjellvåg and P. Norby, *Inorg. Chem.*, 2009, **48**, 1423–1432.
58 M. T. Aytekin Aydın, H. L. Hoşgün, A. Dede and K. Güven, *Spectrochim. Acta, Part A*, 2018, **205**, 503–507.
59 L. Stagi, C. M. Carbonaro, R. Corpino, D. Chiriu and P. C. Ricci, *Phys. Status Solidi*, 2015, **252**, 124–129.
60 M. Salis, P. C. Ricci and A. Anedda, *J. Raman Spectrosc.*, 2009, **40**, 64–66.
61 A. Ould-Hamouda, H. Tokoro, S.-I. Ohkoshi and E. Freysz, *Chem. Phys. Lett.*, 2014, **608**, 106–112.
62 Y. Li, H. Bai, J. Zhai, W. Yi, J. Li, H. Yang and G. Xi, *Anal. Chem.*, 2019, **91**, 4496–4503.
63 L. Mohan and C. Anandan, *Appl. Surf. Sci.*, 2013, **282**, 281–290.
64 L. Mohan and C. Anandan, *Appl. Surf. Sci.*, 2013, **268**, 288–296.
65 C. Anandan and L. Mohan, *J. Mater. Eng. Perform.*, 2013, **22**, 3507–3516.
66 V. V Atuchin, V. G. Kesler, N. V Pervukhina and Z. Zhang, *J. Electron Spectrosc. Relat. Phenom.*, 2006, **152**, 18–24.
67 J. Yan, Z. Lin, C. Ma, Z. Zheng, P. Liu and G. Yang, *Nanoscale*, 2016, **8**, 15001–15007.
68 H. Hernandez-Arriaga, E. Lopez-Luna, E. Martinez-Guerra, M. M. Turrubiartes, A. G. Rodriguez and M. A. Vidal, *J. Appl. Phys.*, 2017, **121**, 64302.
69 B. Bharti, S. Kumar, H.-N. Lee and R. Kumar, *Sci. Rep.*, 2016, **6**, 32355.
70 K. R. Goodman, J. Wang, Y. Ma, X. Tong, D. J. Stacchiola and M. G. White, *J. Chem. Phys.*, 2020, **152**(5), 054714.
71 R. Liu, J. X. Shang and F. H. Wang, *Comput. Mater. Sci.*, 2014, **81**, 158–162.
72 G. Chang, F. Sun, J. Duan, Z. Che, X. Wang, J. Wang, M. J. Kim and H. Zhang, *Acta Mater.*, 2018, **160**, 235–246.
73 H. Tokoro, M. Yoshikiyo, K. Imoto, A. Namai, T. Nasu, K. Nakagawa, N. Ozaki, F. Hakoe, K. Tanaka, K. Chiba, R. Makiura, K. Prassides and S. I. Ohkoshi, *Nat. Commun.*, 2015, **6**, 1–8.
74 J. Lombard, T. Biben and S. Merabia, *J. Phys. Chem. C*, 2017, **121**, 15402–15415.
75 T. S. Santra, C.-W. Chen, H.-Y. Chang and F.-G. Tseng, *RSC Adv.*, 2016, **6**, 10979–10986.
76 L. Mohan, S. Kar, R. Hattori, M. Ishii-Teshima, P. Bera, S. Roy, T. Subhra Santra, T. Shibata and M. Nagai, *Appl. Surf. Sci.*, 2021, **543**, 148815.